

MSene: A new large family of two-dimensional transition metal sulfide with MXene structure

Shu-Xiang Qiao¹, Yu-Lin Han¹, Na Jiao¹, Meng-Meng Zheng¹, Hong-Yan Lu^{1,*}, and Ping Zhang^{1,2}

¹*School of Physics and Physical Engineering, Qufu Normal University, Qufu 273165, China*

²*Institute of Applied Physics and Computational Mathematics, Beijing 100088, China*

Nowadays, discovering new two-dimensional (2D) materials with unique properties and potential applications remains a focus in condensed matter physics. Here, based on first-principles calculations, we report a new large family of transition metal sulfides M_2S with MXene structure in 2H and 1T phases, which we name as MSene. Twenty-four out of fifty-eight MSenes are proved to be stable. Notably, this family includes twelve superconducting (SC) materials, seven SC topological metals (SCTMs), four charge density wave (CDW) materials, and five magnetic materials including one ferromagnetic (FM) and four antiferromagnetic (AFM) materials. For example, 2H-W₂S is a SCTM which exhibits SC transition temperature (T_c) of 12.4 K and nontrivial topological properties as evidenced by topological invariant $Z_2=1$ and the presence of edge states; 1T-Hf₂S is a CDW material with the CDW originating from electron-phonon coupling. The CDW can be suppressed by compressive strain, leading to the emergence of superconductivity; 2H-Cr₂S and 1T-Mn₂S show FM and AFM properties, respectively. Thus, the new large family we predicted shows rich physical properties and significantly expands the repertoire of 2D materials. It serves as a novel platform for investigating the competition or coexistence of multiple orders such as SC, CDW, FM, AFM and topological orders in 2D materials.

Introduction. 2D materials are a general term for a large class of materials with a thickness of only a few atomic layers. Since the successful fabrication of graphene in 2004 [1], 2D systems have garnered significant attention due to their distinctive properties, which differ from corresponding three-dimensional structures. This is due to the confinement of carrier migration and thermal diffusion within the 2D plane. Therefore, they have received widespread attention from the scientific and industrial communities. In recent years, various 2D materials have been investigated, such as hydrides [2–6], carbides [7–14], borides [15–17], nitrides [18–21], transition metal disulfide compounds (TMDs) [22–26], and MXenes [27–30]. These materials typically exhibit outstanding electric, mechanical, catalytic, adsorbing and optical properties, making them a focal point of research in physics, chemistry, and materials science.

TMDs are a widely studied class of 2D materials, encompassing superconductors, semimetals, semiconductors, and insulators, whose chemical formula can be written as MX_2 (M is transition metal, X is chalcogenide element). TMDs possess unique physical properties, including intrinsic magnetism, CDW, and superconductivity, making them highly attractive for applications in high-performance electronic devices, catalysis, and metal electrode contacts [22, 25]. Experimental methods for preparing TMDs are both simple and diverse [31, 32]. For instance, the representative TMD MoS₂ has been successfully fabricated through hydrothermal and thermal decomposition synthesis methods [33], and has lead to wide-ranging applications [34–36].

Apart from TMDs, MXene represents another class of

extensively studied 2D materials [37–40]. MXene can be obtained by selectively separating single atomic metal layers from MAX phase utilizing the differences in properties and relative strength of M-A and M-X bonds [30]. The high electron density of states (DOS) near the Fermi level contributed by transition metals in MXene indicates a high number of electrons [27]. Due to the covalent and ionic mixing properties of M-X bonds within the MXene layer, the interlayer interaction is the van der Waals force, and electrons are usually confined within the plane, resulting in an increased electron mobility and exhibiting metallicity [27]. With its high metal conductivity and excellent chemical stability [37], diverse physical properties of MXene have been experimentally and theoretically investigated, including superconductivity [41–43], band topology [44], and magnetism [45, 46], etc.

Considering the diverse and simple preparation methods of TMDs and good conductivity of MXenes, based on first-principles calculations, this work reports a new large family of transition metal sulfides M_2S (M is transition metal) combining the element composition of TMDs and the stoichiometry of MXenes, and we name it MSene. In the MSene family, we considered all transition metals except for lanthanide and actinide elements and M_2S in 2H and 1T phases, and twenty-four out of fifty-eight materials were found to be stable. Among them, there are twelve SC materials, seven SCTMs, four CDW materials, and five magnetic materials with one in FM and four in AFM ground state. The new large family we predicted greatly enriches the family of 2D materials, and provides a new platform for studying the competition or coexistence of several orders in 2D materials. The predicted MSenes may provide rich applications in condensed matter physics, material physics, and device physics in the future.

Structures and stability. Figures 1(a) and 1(b) depict

*E-mail: hylu@qfnu.edu.cn

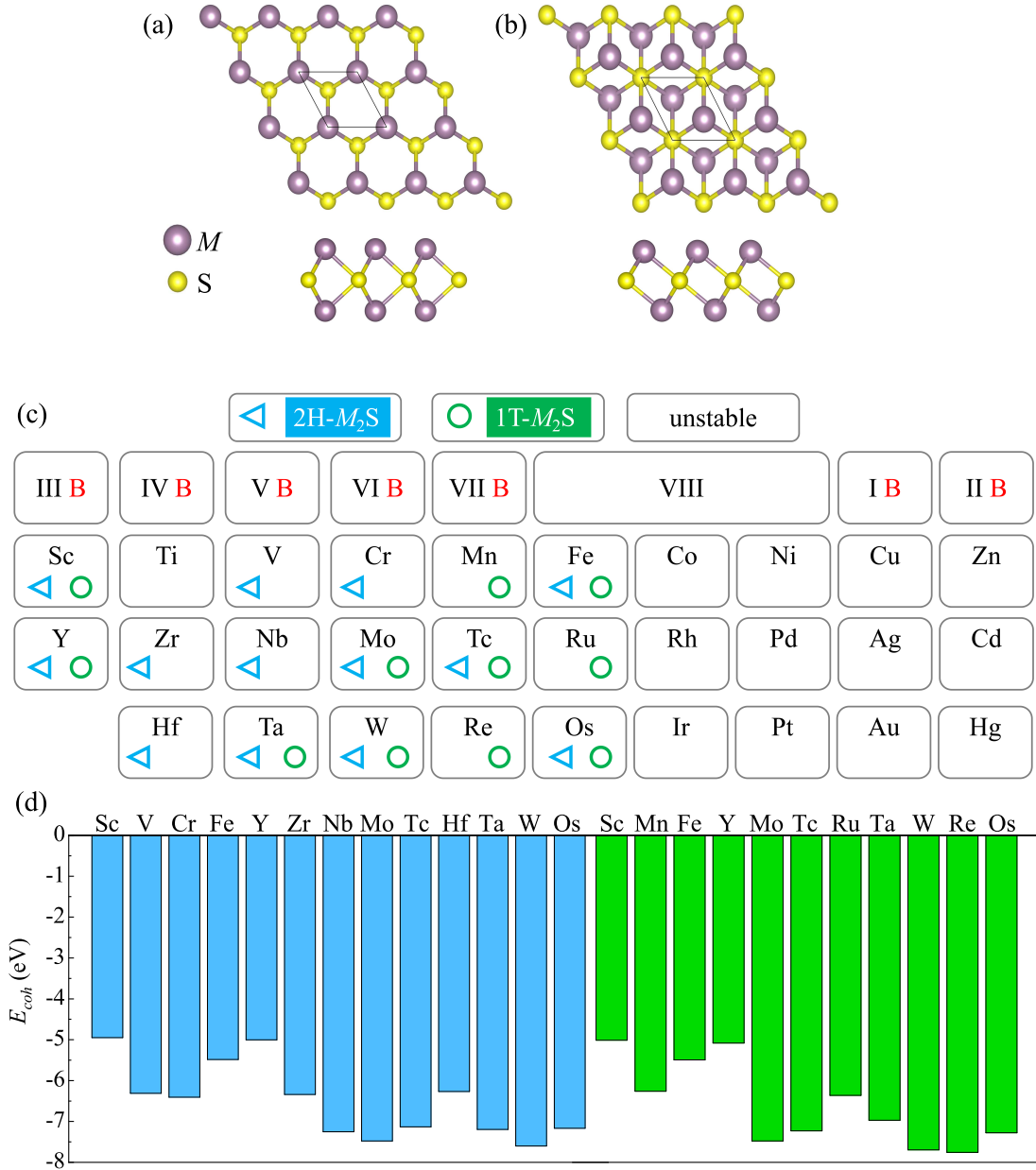


FIG. 1: Top and side views of (a) 2H, and (b) 1T-MSenes. The primitive cell is shown by the black solid line. (c) Distribution of stable 2D MSenes M_2S where M represents transition metal in the periodic table. For clarity, blue triangles and green circles represent stable MSenes in 2H and 1T phase, respectively. (d) The cohesive energies for the MSenes with the M elements labelled above the bars, in which blue and green represents 2H and 1T phase, respectively.

the top and side views of 2H and 1T-MSenes M_2S , where purple spheres represent transition metal (M) and yellow spheres represent S. The space group of 2H- and 1T-MSenes are $P-6m2$ and $P-3m1$, respectively. Unlike Mo_2S , the MSene structure consists of two layers of transition metal atoms and one layer of S atoms sandwiched by M layers. Each primitive cell contains three atoms, including one S atom and two M atoms. The computational methods and details are shown in the Supplemen-

tal Material (SM) [47]. The relaxed lattice parameters of stable MSenes are listed in Table S1 in the SM [47]. The charge density difference in Fig. S1 [47] reveals that M atoms lose electrons while S atoms gain electrons. The electron localization function (ELF) indicates that electrons are distributed around the S atoms, suggesting the formation of ionic bonds, as illustrated in Fig. S1 [47].

Then, we demonstrate the dynamic and thermodynamic stability of MSenes using phonon spectra, cohesive

2H- M_2S				1T- M_2S			unstable												
III B		IV B		V B		VI B		VII B		VIII				I B		II B			
Sc ₂ S		Ti ₂ S		V ₂ S		Cr ₂ S		Mn ₂ S		Fe ₂ S		Co ₂ S		Ni ₂ S		Cu ₂ S		Zn ₂ S	
SC	SC	CDW AFM		SC		FM		CDW AFM	AFM	AFM	SC								
Y ₂ S		Zr ₂ S		Nb ₂ S		Mo ₂ S		Tc ₂ S		Ru ₂ S		Rh ₂ S		Pd ₂ S		Ag ₂ S		Cd ₂ S	
SC	SC	AFM	CDW	SCTM		SCTM	SC	SCTM	SC		SCTM								
		Hf ₂ S		Ta ₂ S		W ₂ S		Re ₂ S		Os ₂ S		Ir ₂ S		Pt ₂ S		Au ₂ S		Hg ₂ S	
AFM	CDW	SCTM	SC	SCTM	SC			SCTM	SC	SC	SC								

FIG. 2: A summary of properties of MSenes. The blue, green and white blocks represent the stable 2H phase, stable 1T phase and unstable structures, respectively. In the blocks, SC, SCTM, CDW, FM and AFM represent SC materials, SC topological metal, charge density wave, ferromagnetism and antiferromagnetism, respectively.

energy E_{coh} , and *ab-initio* molecular dynamics (AIMD) simulations. Figure 1(c) presents a complete diagram of stability information, with blue and green denoting stable 2H-MSenes and 1T-MSenes, respectively. The absence of imaginary frequency in their phonon spectra indicates the dynamic stability, with twenty-four out of fifty-eight 2D MSenes materials identified as dynamically stable ones. The phonon spectra of all MSenes are shown in Fig. S2 [47].

The cohesive energies E_{coh} of dynamically stable MSenes are illustrated in a bar graph in Fig. 1(d), which are calculated using the formula: $E_{coh} = [E_{MSene} - (2E_M + E_S)]/3$, where E_{MSene} , E_M , and E_S represent the total energies of 2H/1T-MSenes (M_2S), isolated M and S atoms, respectively. The values of E_{coh} are provided in Table S2 [47]. Notably, 2H-Hf₂S in this family has been successfully fabricated in experiment [48], and the cohesive energies of most MSenes are lower than that of the experimentally prepared 2H-Hf₂S, as shown in Fig. 1(d) and Table S2 [47]. Furthermore, the calculated cohesive energies of MSenes are lower than some experimentally fabricated 2D materials, such as Cu₂Si (-3.46 eV/atom) [49, 50], GaSe (-2.81 eV/atom) [51], and GaS (-3.62 eV/atom) [51]. AIMD simulations reveal that most MSenes exhibit thermal stability at room temperature and above, as demonstrated in Fig. S3 [47], where the last frame of the photographs for MSenes at the highest stable temperature is displayed. In a word, twenty-four MSenes shown in Fig. 1(c) exhibit good stability, providing promising avenues for future experimental exploration.

After ensuring the structural stability of MSenes, we

discuss interesting and exciting properties of the MSenes family. By analyzing electronic bands and DOS, it is found that they have bands crossing the Fermi level and exhibit metallicity, as shown in Fig. S4 [47]. An overview of the physical properties of stable MSenes is presented in Fig. 2. In the following, we select 2H-Mo₂S, 1T-Hf₂S, 2H-Cr₂S, and 1T-Mn₂S as representatives of SCTM, CDW, FM, and AFM materials for detailed analysis, respectively.

Band topology and superconductivity. The orbital-projected electronic band without spin-orbit coupling (SOC), and the partial density of states (PDOS) of 2H-Mo₂S are shown in Figs. 3(a) and 3(b). It can be observed from Fig. 3(a) that the bands near the Fermi level are mainly contributed by d_{yz} and d_{xz} orbitals. As shown in Fig. 3(b), the contribution of Mo-3d orbitals near the Fermi level is much greater than that of S atoms, thus the metallicity of 2H-Mo₂S is mainly contributed by the Mo- d_{yz}/d_{xz} orbitals. As shown in Fig. 3(c), when SOC is considered, the band near the Fermi level opens a continuous gap, which is highlighted in yellow. The presence of continuous band gap throughout the entire Brillouin zone enables the definition of topological invariants Z_2 . Then, the calculation of the Z_2 yields a value of 1, proving that 2H-Mo₂S is topologically nontrivial. Additionally, the presence of edge states (red trace in Fig. 3(d)) also proves its nontrivial topology. The bands without and with SOC, and edge states of the other six SCTMs are presented in Fig. S5 [47].

The superconductivity of 2H-Mo₂S is investigated with the results shown in Figs. 3(e)-3(i). In Figs. 3(f) and 3(g), phonon DOS (PhDOS) is divided into two dis-

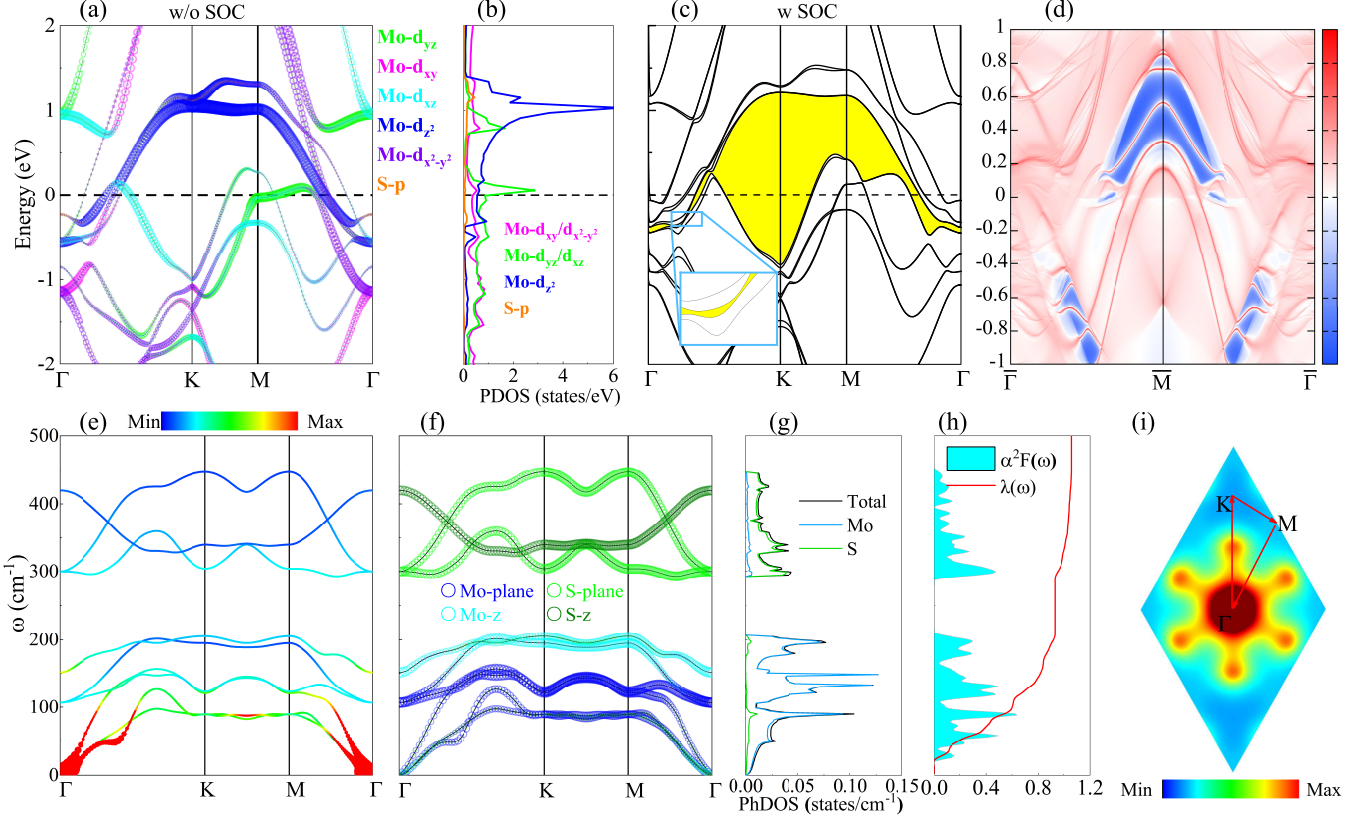


FIG. 3: Band topology and SC properties of 2H-Mo₂S. (a) Orbital-projected electronic band structure without SOC along high-symmetry line Γ -K-M- Γ . (b) PDOS without SOC. (c) Band with SOC. (d) Edge states (red trace). (e) Phonon dispersion weighted by the magnitude of λ_{qv} (EPC for phonon mode qv). (f) Phonon dispersion weighted by the vibration modes of each atom. (g) Phonon DOS. (h) Eliashberg spectral function $\alpha^2F(\omega)$ and EPC $\lambda(\omega)$. (i) The integrated EPC distributions in the plane $q_z = 0$.

trinct regions, with the low-frequency region mainly contributed by the vibration of Mo atoms, while the vibrational modes of S atoms are mainly in the high-frequency region, owing to the larger mass of Mo atoms. As shown in Fig. 3(e), the main contribution of its electron-phonon coupling (EPC) is from acoustic branches around Γ , consistent with Fig. 3(i), and primarily from in-plane vibrations of Mo atoms, as depicted in Fig. 3(f). The strong EPC in the low-frequency region ($\omega < 120 \text{ cm}^{-1}$) contributes 62.4 % to the EPC constant λ as shown in Fig. 3(h). The calculated EPC constant λ and T_c of 2H-Mo₂S are 1.06 and 10.2 K, respectivity. The superconductivity mainly originates from the coupling between Mo- d_{yz}/d_{xz} electrons and the low-frequency in-plane vibration of Mo atoms. Considering that 2H-Mo₂S also show nontrivial topological band structure, it is a potential topological superconductor, which maybe used in fault-tolerant quantum computation.

The phonon spectra weighted by the magnitude of λ_{qv} and Eliashberg spectral function of other SC MSenes are presented in Fig. S6 [47]. These materials all exhibit strong EPC in the low-frequency region. The calculated SC information are summarized in Table S3 [47], including logarithmically averaged phonon frequency ω_{log} , total

EPC constant λ , SC transition temperature T_c , sommerfeld constant γ , specific heat jump at T_c $\Delta C(T_c)$, SC gap at 0 K $\Delta(0)$, critical magnetic field at 0 K $H_c(0)$, isotope coefficient β , and $\frac{2\Delta(0)}{k_B T_c}$. It is noteworthy that the calculated $\frac{2\Delta(0)}{k_B T_c}$ and β of most MSenes are very close to the values given by conventional BCS theory ($\frac{2\Delta(0)}{k_B T_c} \approx 3.53$ and $\beta \approx 0.5$), confirming that MSenes are conventional phonon-mediated superconductors. Moreover, the calculated superconductivity parameters provide reliable data for comparison with future experiments.

CDW property. CDW refers to a periodic fluctuation in charge density that occurs in crystals. It is observed that there are large imaginary frequencies near K and M in the phonon spectrum of 1T-Hf₂S, as depicted in Fig. 4(a), which is a typical phenomenon in CDW materials. CDW primarily originates from two sources: Fermi surface (FS) nesting and EPC. The imaginary part of the electronic susceptibility and the phonon linewidth γ of the lowest acoustic phonon mode are calculated to reveal the source of CDW. Figure 4(b) shows the FS nesting. If the source of CDW is FS nesting, the nesting function exhibits relative maximum at the positions imaginary frequency appears in the phonon spectrum. However, in the

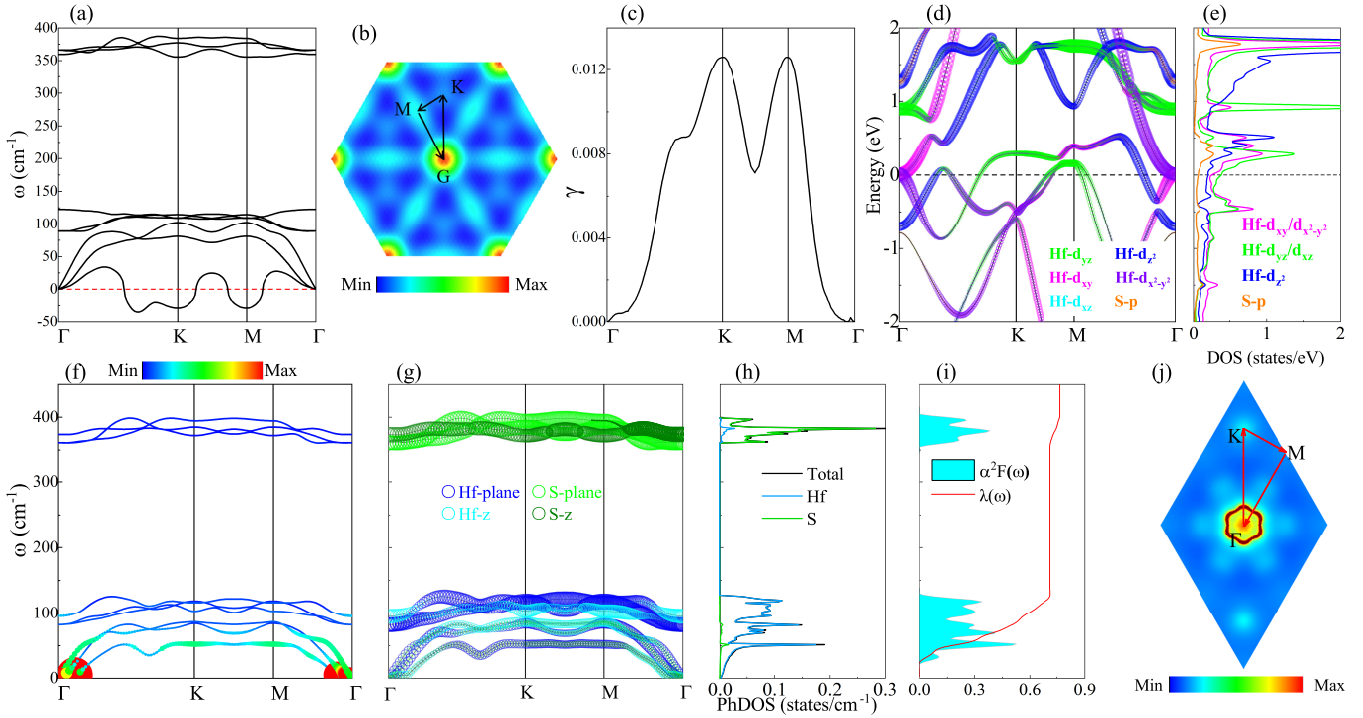


FIG. 4: Properties of pristine 1T-Hf₂S (a-c) and 4% compressive strained 1T-Hf₂S (d-j). (a) Phonon spectrum. (b) Nesting function. (c) Phonon linewidth of the lowest acoustical phonon branch. (d) Orbital-projected electronic band structure. (e) PDOS. (f) Phonon dispersion weighted by the magnitude of $\lambda_{q\nu}$ (EPC for phonon mode $q\nu$). (g) Phonon dispersion weighted by the vibration modes of each atom. (h) Phonon DOS. (i) Eliashberg spectral function $\alpha^2F(\omega)$ and EPC $\lambda(\omega)$. (j) The integrated EPC distributions in the plane $q_z = 0$.

case of 1T-Hf₂S, there is no relative maximum near K and M . Consequently, it can be inferred that the CDW of 1T-Hf₂S does not originate from FS nesting. Then, the phonon linewidth γ of the lowest phonon mode is calculated, which directly reflects the EPC intensity of this branch, as illustrated in Fig. 4(c). It is evident that two peaks are located at K and M , which aligns with the position of the imaginary frequency shown in Fig. 4(a). This correlation indicates that EPC is the origin of CDW in 1T-Hf₂S.

Then, the effect of biaxial compressive strain on CDW is investigated. Biaxial compressive strain is defined as $\varepsilon = (a - a_0)/a_0 \times 100\%$, where a_0 and a represent the lattice constants. The phonon spectrum of 4% compressive strained 1T-Hf₂S is depicted in Fig. 4(f). It is apparent that biaxial compressive strain can suppress CDW. The corresponding electronic states near the Fermi level are mainly composed of Hf- d_{yz}/d_{xz} orbitals and the contribution of S is much smaller, as shown in Figs. 4(d) and 4(e). Due to the competitive relationship between CDW and superconductivity, the superconductivity of 4% compressive strained 1T-Hf₂S is further investigated.

As shown in Figs. 4(f) and 4(i), the EPC around Γ is the strongest, consistent with Fig. 4(j). The strong EPC in the low-frequency region ($\omega < 110 \text{ cm}^{-1}$) contributes approximately 85.2% to the total EPC constant λ . From Figs. 4(d), 4(e), 4(g) and 4(h), it can be seen

that the superconductivity of 1T-Hf₂S mainly originates from the coupling between Hf- d_{yz}/d_{xz} electrons and the low-frequency in-plane orbital vibrations of Hf. The EPC constant λ and T_c of 1T-Hf₂S are 0.77 and 4.5 K, respectively. 1T-Zr₂S shows similar phenomenon to 1T-Hf₂S, and its CDW also originates from EPC. Under 2% compressive strain, the CDW is suppressed and exhibits superconductivity with T_c of 2.1 K, as shown in Fig. S7 [47]. Due to the magnetism of 2H-Ti₂S and 2H-Mn₂S, we do not investigate the complex relationship between magnetism, CDW, and superconductivity in this work, and will study it later.

Magnetic property. Magnetic materials are crucial for various applications. FM materials have important applications in magnetic memory and other fields due to their external magnetic moment. AFM materials can be used as spin electron materials in the field of information storage. As they do not generate a magnetic field and do not interfere with each other, AFM materials can be tightly stacked together to achieve high density storage. Within the MSenes family, 2H-Hf₂S has been experimentally prepared and theoretically predicted to be an AFM material with surface anomalous Hall effect and electric field-induced layer Hall effect [48, 52]. The results for 2H-Hf₂S in this study are consistent with previous research [52]. Additionally, 2H-Cr₂S exhibits FM properties, with the magnetic moment of the Cr atoms on both layers

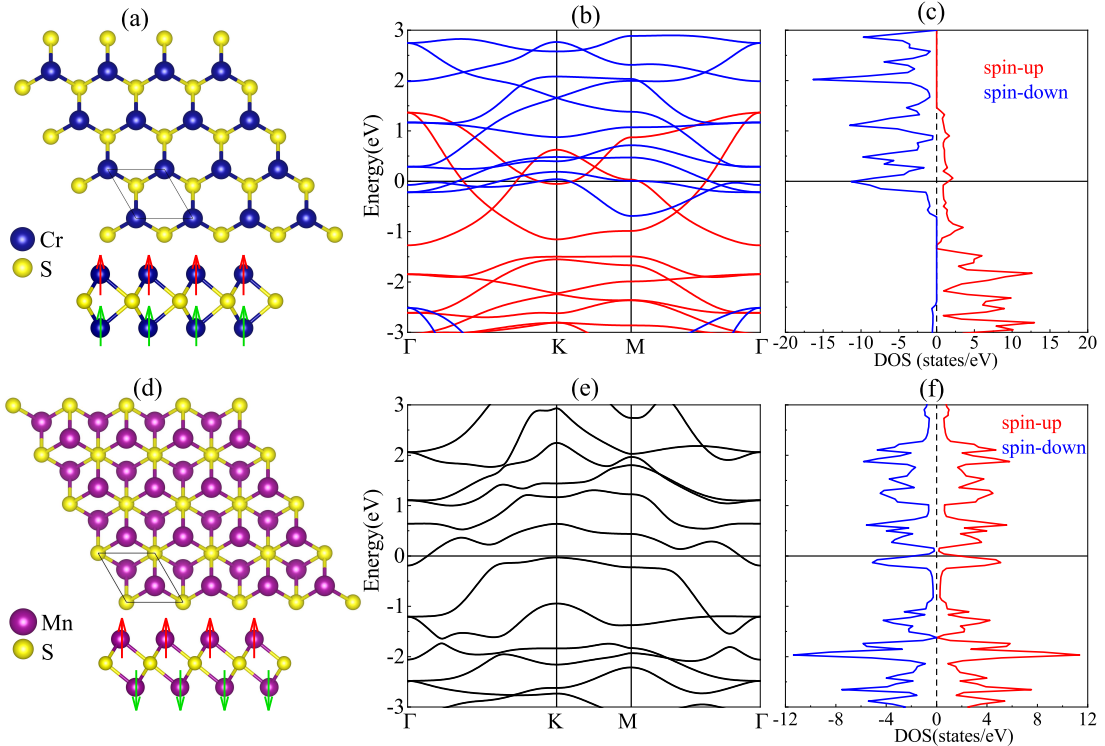


FIG. 5: (a) Top and side views, (b) Band structure, (c) DOS of 2H-Cr₂S. (d) to (f) are similar to (a) to (c), but for 1T-Mn₂S. The arrows in (a) and (d) indicate the the direction of magnetic moment.

pointing in the same direction with the value of $3.3 \mu\text{B}$, as shown in Fig. 5(a). Figs. 5(b) and 5(c) illustrate the band and DOS of 2H-Cr₂S, with red indicating spin-up and blue indicating spin-down. On the other hand, 1T-Mn₂S displays AFM properties, with the magnetic moments of the Mn atoms on both layers being opposite in direction with the value of $3.7 \mu\text{B}$, as shown in Fig. 5(d). Due to the AFM nature, the bands and DOS for spin-up and spin-down overlap with each other in Figs. 5(e) and 5(f). The bands of other magnetic materials are presented in Fig. S4, and their magnetic moments are shown in Table S5 [47]. These results provide theoretical data reference for future experimental research.

Conclusion. In conclusion, we have predicted twenty-four stable MSenes with diverse physical properties, including band topology, superconductivity, CDW, and magnetism. The phonon spectra, cohesive energies, and AIMD fully demonstrate their dynamic and thermodynamic stability. Among them, there are twelve SC materials, seven SCTMs, four CDW materials, and five magnetic materials, including one FM and four AFM. No

tabley, the 2H-W₂S among SCTMs exhibits the highest T_c of 12.4 K in the MSenes, surpassing most TMDs and MXenes. In CDW materials, there is a competition between CDW and superconductivity. The CDW originating from EPC can be suppressed by compressive strain and exhibit superconductivity. Therefore, our results represent a significant breakthrough in 2D sulfide materials and the predicted large MSene family provides a new platform for studying the competition or coexistence of several orders such as SC, CDW, FM, AFM and topological orders in 2D materials.

Acknowledgements. This work is supported by the National Natural Science Foundation of China (Grant Nos. 12074213, and 11574108), the Major Basic Program of Natural Science Foundation of Shandong Province (Grant No.ZR2021ZD01), the Natural Science Foundation of Shandong Provincial (Grant No. ZR2023MA082), and the Project of Introduction and Cultivation for Young Innovative Talentsin Colleges and Universities of Shandong Province.

[1] K. S. Novoselov, A. K. Geim, S. V. Morozov, D. Jiang, Y. Zhang, S. V. Dubonos, I. V. Grigorieva and A. A. Firsov, *Science* **306**, 666–669 (2004).

[2] X. C. Zhou, Y. Hang, L. Liu, Z. H. Zhang, and W. L. Guo, *J. Am. Chem. Soc.* **141**, 7899 (2019).

[3] X. Yan, S. C. Ding, X. H. Zhang, A. Bergara, Y. Liu, Y. C. Wang, X. F. Zhou, and G. C. Yang, *Phys. Rev. B* **106**, 014514 (2022).

[4] J. Bekaert, M. Petrov, A. Aperis, P. M. Oppeneer, and M. V. Milošević, *Phys. Rev. Lett.* **123**, 077001 (2019).

[5] G. Savini, A. C. Ferrari and F. Giustino, *Phys. Rev. Lett.* **105**, 037002 (2010).

[6] Y. J. Chen, H. Y. Lu, F. L. Shao and P. Zhang, *Phys. Rev. Mater.* **7**, 034004 (2023).

[7] Z. H. Zhang, X. F. Liu, B. I. Yakobson, W. L. Guo, *J. Am. Chem. Soc.* **134**, 19326 (2012).

[8] C. Xu, L. Wang, Z. Liu, L. Chen, J. Guo, N. Kang, X. L. Ma, H. M. Cheng, W. Ren, *Nat. Mater.* **14**, 1135 (2015).

[9] C. Si, Z. Liu, W. Duan and F. Liu, *Phys. Rev. Lett.* **111**, 196802 (2013).

[10] S. X. Qiao, C. H. Sui, L. Yang, Y. P. Li, Y. X. Sun, N. X. Zhang, J. Q. Bai, N. Jiao and H. Y. Lu, *Phys. Chem. Chem. Phys.* **24**, 25767 (2022).

[11] Q. Fan, L. Yan, M. Tripp, S. Dimosthenous, S. Kachel, M. Chen, A. Foster, U. Koert, P. Liljeroth and J. M. Gottfried, *Science* **372**, 852-856 (2021).

[12] P. F. Liu, J. Li, C. Zhang, X. H. Tu, J. Zhang, P. Zhang, B. T. Wang and D. J. Singh, *Phys. Rev. B* **104**, 235422 (2021).

[13] G. Profeta, M. Calandra, and F. Mauri, *Nature Phys.* **8**, 131-134 (2012).

[14] H. Y. Lu, Y. Yang, L. Hao, W. S. Wang, L. Geng, M. Zheng, Y. Li, N. Jiao, P. Zhang, and C. S. Ting, *Phys. Rev. B* **101**, 214514 (2020).

[15] Y. V. Kaneti, D. P. Benu, X. T. Xu, B. Yuliarto, Y. Yamauchi, and D. Golberg, *Chemical Reviews* **122**, 1000 (2022).

[16] T. J. Xu, Y. H. Wang, Z. Z. Xiong, Y. T. Wang, Y. J. Zhou, X. F. Li, *Nano-Micro Lett.* **15**, 6 (2023).

[17] Q. C. Li et al., *Science* **371**, 1143 (2021).

[18] H. L. Zhuang, A. K. Singh, R. G. Hennig, *Phys. Rev. B: Condens. Matter Mater. Phys.* **87**, 165415 (2013).

[19] X. T. Jin, X. W. Yan, and M. Gao, *Phys. Rev. B* **101**, 134518 (2020).

[20] H. D. Liu, Y. P. Li, L. Yang, N. Jiao, M. M. Zheng, H. Y. Lu, and P. Zhang, *Phys. Rev. B* **105**, 224501 (2022).

[21] Takat B. Rawal, L. H. Chang, H. D. Liu, H. Y. Lu, and C. S. Ting, *Phys. Rev. Mater.* **6**, 054003 (2022).

[22] S. Manzeli, D. Ovchinnikov, D. Pasquier, O. V. Yazyev, and A. Kis, *Nat. Rev. Mater.* **2**, 17033 (2017).

[23] L. J. Pi, L. Li, K. L. Liu, Q. F. Zhang, H. Q. Li, and T. Y. Zhai, *Adv. Funct. Mater.* **29**, 1904932 (2019).

[24] R. Samal, C. S. Rout, *Adv. Mater. Interfaces* **7**, 1901682 (2020).

[25] B. Zhao, D. Y. Shen, Z. C. Zhang, P. Lu, M. Hossain, J. Li, B. Li, X. D. Duan, *Adv. Funct. Mater.* **31**, 2105132 (2021).

[26] T. Taniguchi, L. Nurdwijayanto, R. Z. Ma, T. Sasaki, *Appl. Phys. Rev.* **9**, 021313 (2022).

[27] M. Naguib, V. N. Mochalin, M. W. Barsoum, Y. Gogotsi, *Adv. Mater.* **26**, 992 (2014).

[28] B. Anasori, M. R. Lukatskaya, Y. Gogotsi, *Nat. Rev. Mater.* **2**, 16098 (2017).

[29] X. T. Jiang, A. V. Kuklin, A. Baev, Y. Q. Ge, H. Ågren, H. Zhang, P. N. Prasad, *Physics Reports* **848**, 1-58 (2020).

[30] A. VahidMohammadi, J. Rosen, Y. Gogotsi, *Science* **372**, 1581 (2021).

[31] F. Yang, P. Hu, F. F. Yang, B. Chen, F. Yin, R. Y. Sun, K. Hao, F. Zhu, K. S. Wang, Z. Y. Yin, *Adv. Sci.* **10**, 2300952 (2023).

[32] S. Joseph, J. Mohan, S. Lakshmy, S. Thomas, B. Chakraborty, S. Thomas, N. Kalarikkal, *Mater. Chem. Phys.* **297**, 127332 (2023).

[33] Kin Fai Mak, Changgu Lee, James Hone, Jie Shan, and Tony F. Heinz, *Phys. Rev. Lett.* **105**, 136805 (2010).

[34] L. Li, Y. K. Zhang, D. X. Shi, G. Y. Zhang, *Acta Phys. Sin.* **71**, 108102 (2022).

[35] R. Ganatra, Q. Zhang, *ACS Nano* **8**, 4074-4099 (2014).

[36] X. Li, H. Zhu, *J Materomics* **1**, 33-44 (2015).

[37] M. Naguib, M. W. Barsoum, Y. Gogotsi, *Adv. Mater.* **33**, 2103393 (2021).

[38] S. Saharan, U. Ghanekar, and S. Meena, *ChemistrySelect* **7**, e202203288 (2022).

[39] K. Khan, A. K. Tareen, M. Iqbal, I. Hussain, A. Mahmood, U. Khan, M. F. Khan, H. Zhang, Z. J. Xie, *J. Mater. Chem. A* **11**, 19764 (2023).

[40] L. M. Malaki, X. T. Jiang, H. L. Wang, R. Podila, H. Zhang, P. Samorì, R. S. Varma, *Chem. Eng. J.* **463**, 142351 (2023).

[41] C. Xu, L. Wang, Z. Liu, L. Chen, J. Guo, N. Kang, X. L. Ma, H. M. Cheng, W. Ren, *Nat. Mater.* **14**, 1135 (2015).

[42] X. Z. Yin, H. Wang, Q. H. Wang, N. Jiao, M. Y. Ni, M. M. Zheng, H. Y. Lu and P. Zhang, *Chinese Phys. Lett.* **40**, 097404 (2023).

[43] H. Wang, X. Z. Yin, L. Yang, Y. P. Li, M. Y. Ni, N. Jiao, H. Y. Lu and P. Zhang, *Phys. Chem. Chem. Phys.* **25**, 22171 (2023).

[44] Y. Liang, M. Khazaei, A. Ranjbar, M. Arai, S. Yunoki, Y. Kawazoe, H. Weng, Z. Fang, *Phys. Rev. B* **96**, 195414 (2017).

[45] S. Chen, Z. Jian and Z. Sun, *ACS Appl. Mater. Interfaces* **7**, 17510 (2015).

[46] G. Gao, G. Ding, J. Li, K. Yao, M. Wu and M. Qian, *Nanoscale* **8**, 8986 (2016).

[47] See Supplemental Material for calculation details, structural parameters, cohesive energy, AIMD, phonon spectra, band, DOS, band topology, superconductivity, CDW and magnetism for stable MSenes.

[48] Kang et al., *Sci. Adv.* **6**, eaba7416 (2020).

[49] L. M. Yang, V. Bacic, I. A. Popov, A. I. Boldyrev, T. Heine, T. Frauenheim and E. Ganz, *J. Am. Chem. Soc.* **137**, 2757 (2015).

[50] B. Feng, et al., *Nat. Commun.* **8**, 1007 (2017).

[51] S. Demirci, N. Avazli, E. Durgun, and S. Cahangirov, *Phys. Rev. B* **95**, 115409 (2017).

[52] J. F. Zhang, D. Xu, X. L. Qiu, N. N. Zhao, Z. Y. Lu, and K. Liu, *J. Phys. Chem. C* **127**, 696 (2023).